

Revisiting the H β Size–Luminosity Relation Using a Uniform Reverberation-Mapping Analysis

SHU WANG ¹ AND JONG-HAK WOO ¹

¹*Department of Physics & Astronomy, Seoul National University, Seoul 08826, Republic of Korea: jhwoo@snu.ac.kr*

ABSTRACT

We revisit the relation between active galactic nucleus (AGN) broad-line region (BLR) size and luminosity by conducting a uniform H β reverberation-mapping analysis for 212 AGNs with archival light curves. Our analysis incorporates three different lag measurement methods, including the interpolated cross-correlation function (ICCF), JAVELIN, and PyROA, alongside a consistently defined lag searching window and an alias removal procedure. We find that ICCF, albeit with larger uncertainties compared to other methods, is the most reliable method based on our visual inspection of the matches between H β and the shifted continuum light curves. Combining this sample with the 32 AGNs from the Seoul National University AGN Monitoring Project, we obtain the best-fit relation between the BLR size (R_{BLR}) and the continuum luminosity at 5100Å (L_{5100}) with a slope significantly flatter than 0.5. By selecting a subsample of 157 AGNs with the best-quality lag measurements using a set of quantitative criteria and visual inspection, we find a consistent slope and a slightly decreased intrinsic scatter. We further investigate the effect of luminosity tracers, including L_{5100} , H β luminosity ($L_{\text{H}\beta}$), [O III] luminosity ($L_{[\text{O III}]}$), and 2 to 10 keV hard X-ray luminosity ($L_{2-10\text{keV}}$). We find that sub-Eddington and super-Eddington AGNs exhibit systematic offsets in the $R_{\text{BLR}}-L_{5100}$ and $R_{\text{BLR}}-L_{\text{H}\beta}$ relation, but are comparable in the $R_{\text{BLR}}-L_{[\text{O III}]}$ and $R_{\text{BLR}}-L_{2-10\text{keV}}$ relation. We discuss the potential causes for these different deviations when employing different luminosity tracers.

Keywords: Active galactic nuclei(16); Quasars(1319); Supermassive black holes(1663); Reverberation mapping (2019)

1. INTRODUCTION

The scaling relation between the mass of supermassive black holes (BHs) and the properties of their host galaxies (e.g., the bulge mass and stellar velocity dispersion) is one of the key ingredients in our understanding of galaxy evolution (Magorrian et al. 1998; Ferrarese & Merritt 2000; Gebhardt et al. 2000; Marconi & Hunt 2003; Häring & Rix 2004; Gültekin et al. 2009; Woo et al. 2010). Exploring the evolution of this relation requires accurate mass determination of distant BHs. However, the traditional method based on stellar/gas dynamics in the BH vicinity becomes impractical due to the insufficient spatial resolution of current observing facilities. One alternative approach is reverberation mapping (RM; e.g., Blandford & McKee 1982; Peterson 1993), which measures the time delay between the continuum variability and the response of broad emission lines, thereby gauging the size of the broad-line region (BLR; R_{BLR}) in active galactic nuclei (AGNs). By combining R_{BLR} and the velocity of BLR gas measured from the line widths, the BH mass can be determined under

the virial assumption, i.e., BLRs are virialized and dominated by the gravitational force of BHs.

Early studies of RM unveiled a scaling relationship between R_{BLR} and continuum luminosity at 5100Å (L_{5100}) (e.g., Kaspi et al. 2000; Bentz et al. 2009). Using a sample of ~ 50 local AGNs with L_{5100} well accounted for host contamination, Bentz et al. (2013) presented a tight $R_{\text{BLR}}-L_{5100}$ relation with a small intrinsic scatter of 0.19 dex, and a slope of $0.533^{+0.035}_{-0.033}$. Their slope was consistent with the expectation from a simple photoionization model. Such a relation significantly simplified the estimation of BH mass, by requiring only single-epoch luminosities and line widths (e.g., Woo & Urry 2002; Vestergaard & Peterson 2006; Shen & Liu 2012; Dalla Bontà et al. 2020). While a variety of emission lines were utilized for AGNs at different redshifts, the H β $R_{\text{BLR}}-L_{5100}$ relation has been best studied with the local RM sample, providing the foundation of all other virial BH mass estimators beyond the local universe.

However, more recent RM studies, which extended to a broader range of both luminosities (e.g., Grier et al. 2017; Li et al. 2021; Woo et al. 2024) and Eddington ra-

tios (e.g., Wang et al. 2014b; Du et al. 2014, 2015, 2016, 2018; Hu et al. 2021), reported a significant increase in the scatter of the $R_{\text{BLR}}-L_{5100}$ relation. In particular, super-Eddington AGNs show a significant offset from the $R_{\text{BLR}}-L_{5100}$ relation of sub-Eddington AGNs. By adding 32 AGNs with moderate-to-high luminosity, Woo et al. (2024) found that the current $R_{\text{BLR}}-L_{5100}$ relation is characterized by a shallower slope of ~ 0.4 and a larger intrinsic scatter of 0.23 dex than that of Bentz et al. (2013). In addition, the independent observation from GRAVITY confirmed the shallower slope of $R_{\text{BLR}}-L_{5100}$ relation based on a small sample of AGNs with spectro-interferometric observations (GRAVITY Collaboration et al. 2024a).

For understanding the systematic trends in the relation, Du & Wang (2019) reported a strong correlation between the deviation from $R_{\text{BLR}}-L_{5100}$ relation and the Fe II to $\text{H}\beta$ flux ratios, which is commonly used as an indicator of accretion rate (e.g., Shen & Ho 2014). It means that the higher the accretion rate is, the more the BLR size is shortened, which could be explained by the self-shadowing effect of the slim accretion disk (Wang et al. 2014a). The inner part of the slim disk is puffed-up and partially obscures the ionizing photons that illuminate the BLRs, resulting in the overall shortening of R_{BLR} . Woo et al. (2024) demonstrated that the flattening of the relation is related to the higher average Eddington ratios at higher-luminosity bins. In addition, Fonseca Alvarez et al. (2020) suggested that the deviation likely depends on the UV/optical spectral energy distribution, i.e., the ratio between the optical and the ionizing luminosity. By using the ratio between [O III] and $\text{H}\beta$ as the proxy for UV ionizing photons, they demonstrated that the changing in UV to optical SEDs may also contribute in the offset and scatter of the $R_{\text{BLR}}-L_{5100}$ relation.

While our understanding of the $R_{\text{BLR}}-L_{5100}$ relation has significantly deepened with the growing RM sample, it is important to note that the $\text{H}\beta$ lags reported in the literature were not measured uniformly, which could introduce extra scatter that complicates the comprehension. Some lags were measured based on the interpolated cross-correlation function (ICCF) (Peterson et al. 1998), while others were based on JAVELIN (Zu et al. 2011). These two approaches can have significant difference in the lag uncertainty estimation (Li et al. 2019; Yu et al. 2020b), and their lags can also be inconsistent (e.g., Woo et al. 2024). Thus, it is of importance to conduct a uniform lag analysis for testing the effect of different lag measurement methods. In addition, there is a range of the reliability of the reported lags in the literature, owing to the diverse quality of light curve data

and adopted analysis. It is important to test whether the observed scatter of $R_{\text{BLR}}-L_{5100}$ relation can change with a more rigorously selected sample with the best quality lag measurements.

In this paper, we perform a uniform analysis to re-measure $\text{H}\beta$ lag for a large sample of the previously reverberation-mapped AGNs in the literature, and revisit the R_{BLR} -luminosity (L) relation using different luminosity tracers. We summarize the AGN sample and light curve data collection in §2. In §3, we investigate the influence of different lag measurement methods and lag qualities on $R_{\text{BLR}}-L_{5100}$ relation. In §4, we study impact of the different luminosity tracers and discuss our current understanding of the $R_{\text{BLR}} - L$ relation in §5. In §6, we give a brief summary of our findings. Throughout this paper, we use the Λ CDM cosmology, with $H_0 = 72.0$, and $\Omega_m = 0.3$.

2. SAMPLE AND DATA COLLECTION

2.1. Sample

The sample used in work consists of two parts. First, we collected all AGNs with $\text{H}\beta$ RM measurements published before 2022 (literature master sample), where we found ~ 280 individual lag measurements. Second, we incorporated the lags of 32 moderate-to-high-luminosity AGNs from the Seoul National University AGN Monitoring Project (SAMP; Woo et al. 2019; Woo et al. 2024).

For the literature master sample, we collected the $\text{H}\beta$ and continuum light curves for each object from the original papers to perform a uniform lag analysis. In this process, we removed objects for which the two light curves were not available. In some cases, we applied small adjustments to the archival light curves whenever required, e.g., excluding outliers and inter-calibrating between different bands or telescopes, following the guidance from the original papers. We also collected the lags reported in the literature ($\tau_{\text{literature}}$) for comparison purposes.

To investigate the $R_{\text{BLR}}-L_{5100}$ relation, we also collected the host-corrected AGN continuum luminosity L_{5100} . The host contamination can be estimated based on space/ground-based image decomposition (e.g., Bentz et al. 2013), spectral decomposition or empirical relations (e.g., Shen et al. 2011). We excluded 38 objects, for which any host galaxy correction is not available. We mainly collected the L_{5100} from the database of Bentz & Katz (2015) and supplemented this database with the additional new measurements from Dalla Bontà et al. (2020) as well as other individual papers. We revised these luminosities with the same cos-

mological parameters, except for very nearby AGNs, for which the direct distance measurements were adopted.

In addition we excluded 28 unreliable lag measurements due to the under-sampling or low variability as reported by the previous works (Bentz & Katz 2015). Thus, we finalized the remaining 212 AGNs with H β RM measurements as the literature parent sample for the following lag analysis. For clarity, we assigned an ID to each AGN in this sample (see Table A.1 in the Appendix for details).

Table 1. Sample Collection

Sample	N_{objects}
Literature master sample	280
Light curves not available	2
Host-subtracted luminosity not provided	38
Previously identified as un-reliable lags	28
Literature parent sample	212
SAMP	32
Total sample	244

Then we combined the literature parent sample with the 32 moderate-to-high-luminosity AGNs from SAMP. The measured lags based on ICCF and JAVELIN are presented by Woo et al. (2024), along with the host-corrected L_{5100} based on spectral decomposition. Note that we adopted a similar methodology and lag quality assessment as Woo et al. (2024). The final total sample contains 244 AGNs (see Table 1).

2.2. Other Properties

We collected several spectral properties for the literature parent sample, including broad H β luminosity ($L_{\text{H}\beta}$), [O III] luminosity ($L_{[\text{O III}]}$), the line dispersion (σ_{line}) measured from the root-mean-square (rms) spectra, and the full-width-at-half-maximum (FWHM) measured from the mean spectra. The $L_{\text{H}\beta}$ is a direct product of BLR ionization, thus is a good indicator of the ionizing luminosity. It is also less subject to the difficulty in removing the host galaxy contribution (Dalla Bontà et al. 2020). The $L_{[\text{O III}]}$ may reflect the amount of higher energy photons because [O III] has an ionization potential of ~ 55 eV. For the majority of our sample, these measurements were collected from Du & Wang (2019); the properties for the Sloan Digital Sky Survey – RM (SDSS–RM) were collected from Shen et al. (2019); the properties of SAMP AGNs were measured by this work.

We also collected the velocity dispersion measured from rms spectra ($\sigma_{\text{line,rms}}$) for calculating the BH mass

and the Eddington ratio (λ_{Edd}). The $\sigma_{\text{line,rms}}$ is primarily used for M_{BH} calculation, because it is generally more consistent with the virial assumption (Peterson et al. 2004; Park et al. 2012; Wang et al. 2020) and less subject to orientation effect (e.g., Collin et al. 2006; Wang et al. 2019; Yu et al. 2020a). For objects with no available $\sigma_{\text{line,rms}}$, the $\text{FWHM}_{\text{mean}}$ were adopted. We adopted a single representative virial coefficient $f = 4.47$ for $\sigma_{\text{line,rms}}$ and $f = 1.12$ for FWHM (Woo et al. 2015).

3. INVESTIGATION OF UNIFORM LAG MEASUREMENT

3.1. Lag measurement

Two lag measurement methods are primarily adopted in the literatures, i.e., ICCF (e.g., Gaskell & Peterson 1987; Peterson et al. 1998) and JAVELIN (Zu et al. 2011). ICCF is a non-parametric, model independent method, while JAVELIN is based on the damped random walk model (Kelly et al. 2009). Detailed comparison between these two methods have been performed based on simulated light curves (Li et al. 2019; Yu et al. 2020b). The results show that both methods are generally robust. However, ICCF tends to overestimate the lag uncertainty than the value determined from random trails, while JAVELIN is more susceptible to the underestimation of the light curve flux uncertainties. In this work, we compare these methods using archival light curves from real observation. In addition, we supplement our analysis with a third approach PyROA (Donnan et al. 2021), which is recently developed based on a different methodology and is also effective in recovering lags (Shen et al. 2023; Khatu et al. 2023). In the following, we briefly outline the methodology of these methods and the parameter setting.

ICCF measures the cross-correlation function (CCF) using linear interpolation. Specifically, at each step τ of a lag searching array, one light curve is shifted by τ and linearly interpolated on the time grid of the other. The Pearson cross-correlation coefficient r is calculated between the interpolated first light curve and the second light curve. This process is repeated over the entire lag searching array, providing r as a function τ , which is called as ICCF. Exchanging the order of the first and second light curve results in two ICCFs, and the final ICCF is the average of these two.

The ICCF lag measurement can be derived from either the peak or the centroid of ICCF, with the latter considered as the more robust measure (Peterson et al. 2004) which is adopted in this work. Specifically, the ICCF centroid is calculated using points with $r \geq 0.8r_{\text{max}}$ (Peterson et al. 2004) around the r_{max} . By employing the Flux Randomization (FR) and Random Subset

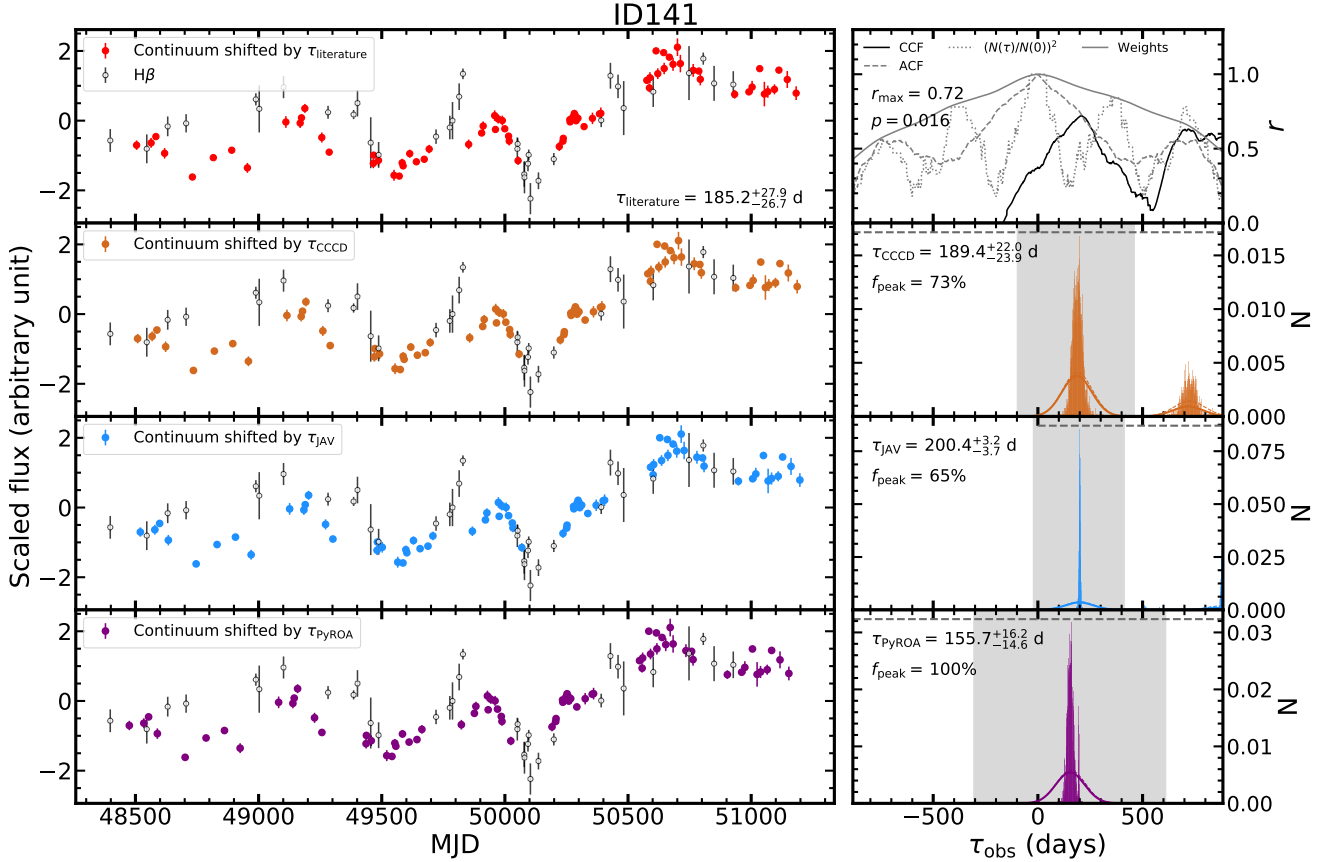


Figure 1. Example of lag measurements based on ICCF, JAVELIN, and PyROA for ID141. Left: the $H\beta$ light curve (black open circles) is compared to the continuum light curve shifted by $\tau_{\text{literature}}$ (top panel; red circles), τ_{ICCF} (second panel; brown circles), τ_{JAV} (third panel; blue circles), and τ_{PyROA} (bottom panel; purple circles), respectively. Right: Top panel: the CCF (black solid line) and weighting functions, including the ACF (grey dashed line), overlapping function (grey dotted line), as well as the final weights (grey solid line; see §3.2 for details). The r_{max} and p -value are also labeled at the left, which describe the correlation strength and the significance of the correlation, respectively (see §3.5 for more details). Second to bottom panels: the posterior distribution of τ_{ICCF} (second panel), τ_{JAV} (third panel), and τ_{PyROA} (bottom panel). The dashed and solid curves represent the smoothed unweighted and weighted distribution, respectively. The grey shaded area illustrates the range of the primary peak. The lag measurement as well as the fraction (f_{peak}) of the posterior distribution within the primary peak is labeled at the left. The horizontal dashed lines at the top represent the lag searching window adopted for this object. Complete figures for each object are presented online in their entirety.

Selection (RSS) methods, we generate 5000 realizations of the light curves and obtain the sampling distribution. The details of the FR and RSS approach are described in Peterson et al. (1998) and implemented by the package PyCCF (Sun et al. 2018). In the following text, we ignore the difference between posterior distribution and sampling distribution, while acknowledging that the ICCF outputs are actually different from posterior distribution based on Markov Chain Monte Carlo (MCMC) techniques.

JAVELIN utilizes the damped random walk (DRW) model (Kelly et al. 2009) to simulate and interpolate light curves. It describes the emission-line light curve as a shifted, smoothed version of the continuum light curve

(Zu et al. 2011) using a top-hat transfer function. The best-fit parameters of the DRW model and the transfer function are determined using MCMC techniques. In this work, we utilize the JAVELIN v0.33 and adopt the $n_{\text{burn}} = n_{\text{walk}} = 100$ and $n_{\text{chain}} = 300$ as the MCMC parameters.

PyROA utilizes the running optimal average (ROA) to model light curves (Donnan et al. 2021) which represents an inverse-variance weighted average of all data points. It is an empirical method without assumption of the DRW model. The fitting is performed on the stacked light curves which are merged from the continuum and the shifted and scaled $H\beta$ light curves. The ROA model is multiplied with a Gaussian window function with a

width of Δ to suppress influence from distance points. The best-fit model is derived by balancing the goodness of the fit (i.e., χ^2) and the effective number of parameters which is a function of Δ . The model parameters are determined using Bayesian analysis. In this work, we adopted $N_{\text{sample}} = 10000$ in the MCMC calculation and $[5.0, 30.0]$ days as the Δ range. In a small number of cases, the Δ range is adjusted to prohibit overfitting with a small Δ value. As for the initial guess of the lag for PyROA, we utilize the ICCF lag as an input.

Next, we describe how we define the lag searching windows. In principle, a longer lag searching window is able to search for more possibilities, while in practice it results in more aliases and even a failure in recovering the real lag. In this work, the light curve from campaigns with different length focusing on objects with different lags, which makes it difficult to find a uniform optimal solution for each object. After testing several different options based on the time baseline length, we decide to use the lag searching window as ± 0.33 times of the baseline for ICCF and PyROA, which is similar to what is adopted by Woo et al. (2024). For JAVELIN, we use $[0, +0.33]$ times of the baseline as the searching window because we find that symmetric windows often cause negative lag measurements that are not physically meaningful. Most of these adopted searching windows are larger than the expected lags from the $R_{\text{BLR}}-L_{5100}$ relation of Bentz et al. (2013). However, there are 15 objects whose expected lags from Bentz et al. (2013) are larger than our lag searching windows. For these targets, we additionally use ± 0.5 times of the baseline as the searching window and found that the ICCF result doesn't change. We argue that employing larger windows can result in lags that are less reliable, because such lags lead to smaller overlap between the shifted continuum and $H\beta$ light curves using the lag.

3.2. Alias removal

Next, we describe our methodology of removing aliases in the posterior distributions. All these three approaches can show multiple peaks in their posterior distribution due to the limited time sampling and baseline length, quasi-periodic variability, and etc. (Grier et al. 2017; Homayouni et al. 2020). The situation can be more severe when there are large seasonal gaps in the light curves. In these cases, applying a weighting function to suppress and remove the alias is necessary.

We first smooth the posterior distribution using a Gaussian kernel whose width is empirically determined to be 0.075 times of the baseline length of the continuum light curves. This value is determined by visual inspection of the smoothed posterior distribution. Then the

smoothed posterior distribution is multiplied with the weights as demonstrated in Figure 1. Similar to those applied by Grier et al. (2019), the weights consists of two components: the auto-correlation function (ACF) the overlapping function. The ACF reflects the rapidity of the variability, where a narrow ACF reflect rapid variability where the lag is more easily affected by the seasonal gap. The overlapping function is calculated by $P(\tau) = (N(\tau)/N(0))^2$, where $N(\tau)$ is the number of overlapping points between the two light curves after shifting the continuum light curve with τ . At specific τ , the overlapping points are defined as those $H\beta$ -shifted continuum epoch pairs for which the time difference is less than twice the median cadence of the continuum light curves. We follow the approach by Grier et al. (2017) to clip ACF at its first zero-point (if any) surrounding $\tau = 0$, and the final weights is the convolution between the clipped ACF and the overlapping function $P(\tau)$.

The primary peak is defined as the highest peak in the weighted smoothed posterior distribution, and its range is determined as the two adjacent local minima around the primary peak or the searching window if no local minimum is found. The final lags are determined from the unweighted posterior distribution that are inside the primary peak range.

3.3. Detrending

We explore the effect of removing the long-term trend, a process known as detrending, on the lag measurements. The presence of a long-term trend can skew the lag measurement (Peterson et al. 1995), and moreover, the different long-term trends in the continuum and $H\beta$ light curves can reduce the correlation strength (Zhang et al. 2019; Li et al. 2020). We perform a test to detrend both the continuum and $H\beta$ light curves using linear function, where the best-fit linear trend is subtracted in both light curves. We perform ICCF calculation on the detrended light curves. While for most objects the correlation strength becomes weaker, ~ 20 objects show stronger correlation strength. We find that most of these objects show consistent lag measurements before and after detrending. Only five of them show inconsistent lags at 3σ level, e.g., 3C 273 (Zhang et al. 2019). Based on our visual inspection, we adopt the lags with the detrending when the r_{max} is improved by 0.1 and the lags are inconsistent at 3σ level before and after the detrending.

3.4. Lag comparison

We present the lag measurements of the literature parent sample based on the three methods in Table A.1. In

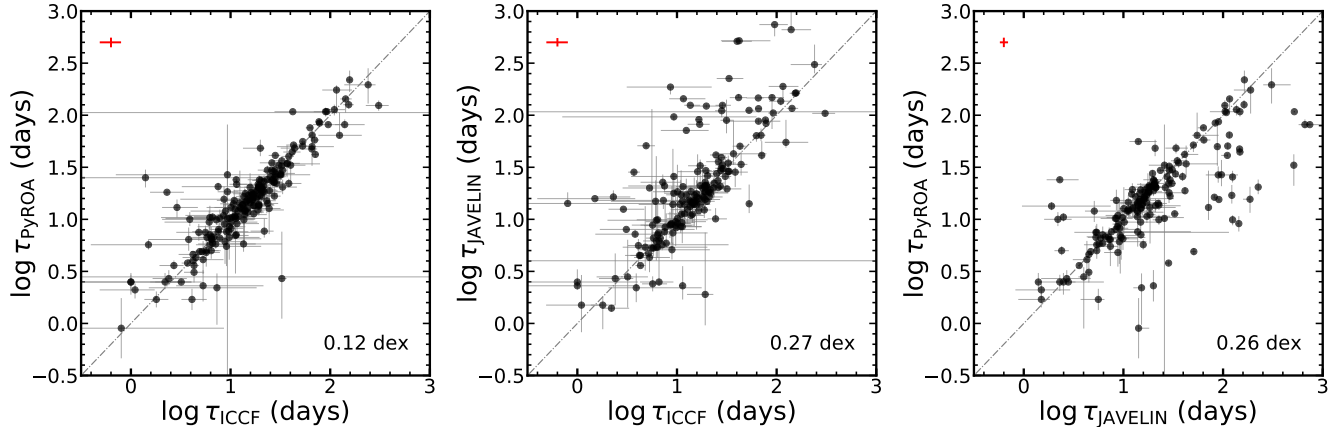


Figure 2. Comparison between τ_{ICCF} , τ_{JAV} , and τ_{PyROA} . The grey dotted dashed line represents the 1:1 relation. The red crosses at the top left corner indicate the median uncertainties of x- and y-axis. The scatter in 16-to-84th percentile range is shown at the bottom right corner.

Figure 2, we compare the the lags from these methods (i.e., τ_{ICCF} , and $\tau_{JAVELIN}$, and τ_{PyROA}). In the comparison, we remove those lags that are not converged or affected by the boundary of lag searching windows. We find that (1) τ_{ICCF} and τ_{PyROA} are mostly consistent with each other; (2) while for most objects $\tau_{JAVELIN}$ is consistent with other two lags, there are many outliers.

To examine the outliers and determine which measurements might be problematic, we shift the continuum light curves according to the lags of each of these three methods, and align the flux based on the median and standard deviation (Figure 1). Visual inspection of these figures suggests that the discrepancy is primarily associated with inaccurate $\tau_{JAVELIN}$, while τ_{ICCF} (and τ_{PyROA}) generally yield a better match between the light curves. For some objects, for example, ID057 and ID062, $\tau_{JAVELIN}$ matches the continuum and $H\beta$ light curves in the seasonal gap, leading to almost no overlap between these two.

Similar results have been observed in several monitoring campaigns with multi-year baseline and moderate cadence (Shen et al. 2023; Woo et al. 2024). These works find that the failed $\tau_{JAVELIN}$ often match the two light curves in the seasonal gaps. This tendency of JAVELIN to favor lags close to the length of seasonal gaps may arise from its inadequate handling of underestimated flux uncertainties. When the flux is imprecise and its uncertainty is underestimated, JAVELIN’s best solution tends to minimize the overlap to reduce the mismatch. In addition, we find that some $\tau_{JAVELIN}$ are not converged, which is not seen in the case of ICCF and PyROA. These results suggest that ICCF and PyROA are generally more reliable than JAVELIN.

Despite that τ_{ICCF} are generally reliable, there are some cases where $\tau_{JAVELIN}$ or τ_{PyROA} are more accurate,

presenting better matches between $H\beta$ and the shifted continuum light curves than τ_{ICCF} . Such cases include ID 074, ID 133, and ID 145. A common feature of these objects is that there is a primary non-linear long-term trend, e.g., a bowl-like structure, in their light curves. In this case, their τ_{ICCF} are sometimes overestimated. On the contrary, the other two lags can successfully match the feature in the light curves. It implies the need for more complex detrending to obtain unbiased ICCF lag measurements for such objects.

For lag uncertainties, we find that the uncertainty of τ_{ICCF} is about 2.2 and 2.1 times larger than that of τ_{PyROA} and $\tau_{JAVELIN}$, respectively. This finding is consistent with the results based on simulated light curves (Li et al. 2019; Yu et al. 2020b). Yu et al. (2020b) reports that ICCF typically overestimates the ‘true’ uncertainty—calculated from random realization of the original light curve—by a factor of approximately 3, while JAVELIN only slightly overestimates the ‘true’ uncertainty by 1.1 times. As for the comparison between the τ_{PyROA} and $\tau_{JAVELIN}$, the uncertainty of $\tau_{JAVELIN}$ is about 1.1 times larger than that of PyROA.

Combining these results, it seems that τ_{PyROA} is the best option, given the reliable lag measurements and small lag uncertainties. However, it’s important to note that we utilize τ_{ICCF} as initial values in τ_{PyROA} calculations. Consequently, it’s natural for τ_{PyROA} to demonstrate better consistency with τ_{ICCF} than $\tau_{JAVELIN}$. To assess this effect, we conduct an experiment using $\tau_{JAVELIN}$ as the initial value in PyROA calculation. This test reveals that for some objects, the recalculated τ_{PyROA} shift to more closely align with $\tau_{JAVELIN}$, especially when $\tau_{JAVELIN}$ and τ_{ICCF} exhibit significant discrepancies. It suggests the τ_{PyROA} of the current version is dependent on the initial values. Furthermore, for some

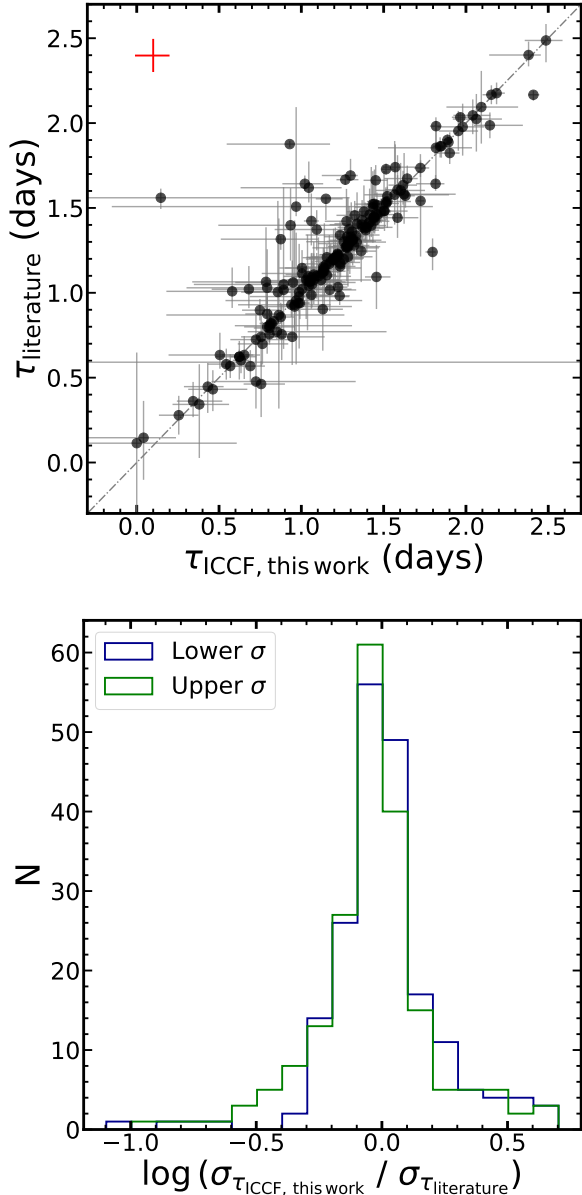


Figure 3. Upper: comparison between the lags originally reported in the literature ($\tau_{\text{literature}}$) and the lags measured in this work based on ICCF ($\tau_{\text{ICCF, this work}}$). The grey dotted-dashed line represents the 1:1 correspondence. The red cross at the top-left corner indicates the log scale average uncertainty of both axes. Lower: distribution of the difference between the lag uncertainty of $\tau_{\text{literature}}$ and the uncertainty of $\tau_{\text{ICCF, this work}}$. Lower and upper uncertainties are shown using blue and green color, respectively.

objects with relatively low cadence, we have to manually adjust the Δ range in PyROA calculations to avoid over-fitting caused by small Δ values. Therefore, τ_{ICCF} provides the most robust lag measurements.

In the subsequent analysis, we adopt τ_{ICCF} as our final lag measurement, despite it having larger uncertainties

than the other two methods. Note that τ_{PyROA} is also utilized to evaluate how the lag uncertainties may affect the intrinsic scatter of the $R_{\text{BLR}}-L_{5100}$ relation.

As a consistency check, we compare our new lag measurements (τ_{ICCF}) with those originally reported in the literature in Figure 3. The two measurements are mostly consistent with each other and their uncertainties also show no large difference. This general consistency is expected in the sense that ICCF is the primary method used in the literature. There are some objects whose new lag uncertainties are larger than the previously reported values, owing to the larger searching window or a different lag measuring method. While our new measurements are generally consistent with the previously reported ones, we uniformly determine the lag and uncertainty of the large sample, providing a valuable database for future works.

3.5. Quality Assessment

3.5.1. Literature Sample

In this section, we perform a quality assessment for the literature sample by setting several criteria, which were similarly applied by Woo et al. (2024). We focus on the quality assessment of τ_{ICCF} as it is adopted as the primary lag measurement. First, we require that the maximum correlation coefficient r_{max} is larger than 0.55. This threshold is determined based on our visual inspection, and is similar to the value used in the literature, e.g., 0.5 or 0.6 (Grier et al. 2017; U et al. 2022; Woo et al. 2024).

Second, we check the significance of the correlation, which is also affected by the variability amplitude and the presence of strong variability features. To quantify it, we generate random H β light curves and study the possibility of these mock light curves having the same or stronger correlation than the observed one. Specifically, we generated 1000 mock H β light curves for each object with flux randomized at each point but keep the same sampling pattern as the original light curves. Then a linear trend that was derived from the fitting of original H β light curves was added to these random emission-line light curves. These mock H β light curves were then cross-correlated with the observed continuum light curves, and the results were compared with the those from real observation. With 1000 realizations, we calculated the p -value as the fraction of the the mock realization having r_{max} larger than the observed r_{max} . The smaller the p -value is, the higher the significance of the correlation is. However, there is not a clear threshold for this p -value to indicate the significance level. We empirically chose p -value equal 0.1 as the threshold.

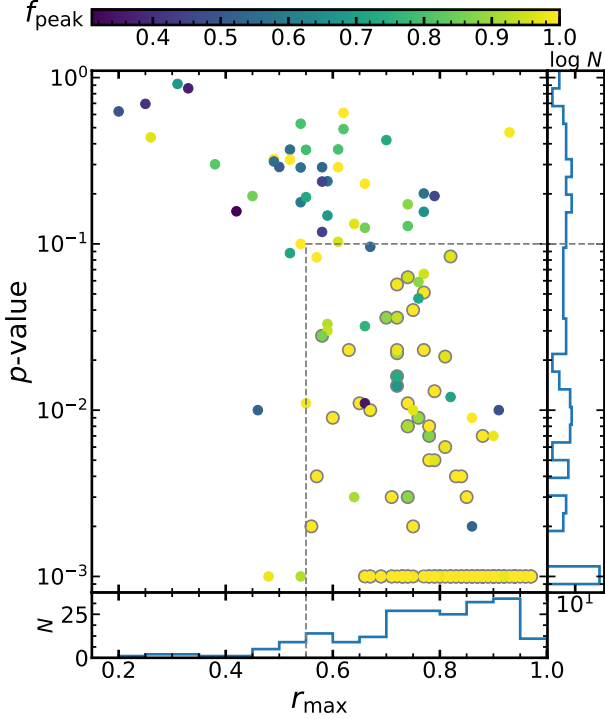


Figure 4. Demonstration of our selection for the best quality lag measurements. The literature parent sample (212 objects) are plotted on the r_{\max} - p -values plane, and color-coded by the f_{peak} of the τ_{ICCF} . Objects with $r_{\max} > 0.55$, $p\text{-value} \leq 0.10$ (as indicated by the grey dashed lines), and $f_{\text{peak}} \geq 0.6$ are selected as good-quality lag measurements. The histogram of both r_{\max} and p -values are also displayed in the bottom and right panel, respectively. In addition, we perform visual assessment on the lag quality. Those objects selected based on our visual inspection are denoted with circles with grey edges.

Table 2. Selection of Best-quality Lag Measurements for Literature Sample

Sample	N_{objects}
Literature parent sample	212
$\tau_{\text{ICCF}} - \sigma_{\tau_{\text{ICCF}}} > 0$	197
$r_{\max} > 0.55$, $p\text{-value} \leq 0.10$, $f_{\text{peak}} \geq 0.6$	156
Removed by visual inspection	22
Best-quality literature sample	134

Third, we performed a quality assessment (QA) by visually inspecting the goodness of the match between $\text{H}\beta$ and shifted continuum light curves (based on the τ_{ICCF}), as well as the posterior distribution. The specific factors we considered include the follows:

- There are obvious variability features (beyond the linear trend) that are clearly matched between $\text{H}\beta$ and the shifted continuum light curves.
- The overlapping fraction between $\text{H}\beta$ and the shifted continuum light curves is large, at least enough to cover the several variability features, which is necessary to avoid random correlation. The cadence is sufficient to describe the variability features.
- The CCF has a clear peak around the measured τ_{ICCF} . Note that a flat CCF or a CCF with multiple peak may indicate ambiguous lag measurements.
- The primary peak in τ_{cent} posterior distribution is well defined, i.e., no other strong peaks outside the primary peak range, no connected sub-peaks inside the primary peak ranges. The primary peak is not affected by the boundary of the lag searching window.

We present the result of our quantitative assessment in Figure 4 and summarize the number of objects in each selection step in Table 2. Adding additional visual inspection only slightly reduces the sample size. Note that this further selection based on visual inspection does not affect the $R_{\text{BLR}}-L_{5100}$ relation. By combining the quantitative criteria and the visual inspection, we finally obtain the best-quality literature sample, which consists of 134 lag measurements.

3.5.2. Best-quality Lags From SAMP

Woo et al. (2024) measured 32 $\text{H}\beta$ lags from SAMP, in which 30 objects show significantly positive lags ($1\sigma > 0$) based on τ_{ICCF} . SAMP τ_{ICCF} are measured using a searching window of $\sim 30\%$ of the baseline ($[-600, 600]$ days), which typically exceeds twice of the expected lags predicted from the canonical $R_{\text{BLR}}-L_{5100}$ relation (Bentz et al. 2013). They applied the same alias removal procedure as we described above. However, Woo et al. (2024) didn't conduct PyROA analysis. Consequently, we measure τ_{PyROA} for these AGNs, adhering the same parameter setting previously mentioned, such as the adoption of τ_{ICCF} as initial values. These τ_{PyROA} measurements are summarized in the Appendix.

Woo et al. (2024) performed a quality assessment on τ_{ICCF} and selected a subsample with good-quality lag measurements, using three criteria: (1) $r_{\max} > 0.6$; (2) $p(r_{\max}) \leq 0.20$; (3) $f_{\text{peak}} \geq 0.6$. Note that their $p(r_{\max})$ is different from the p -value calculated in this paper. To calculate the p -value, Woo et al. (2024) utilizes the DRW model to generate the random light curves (U

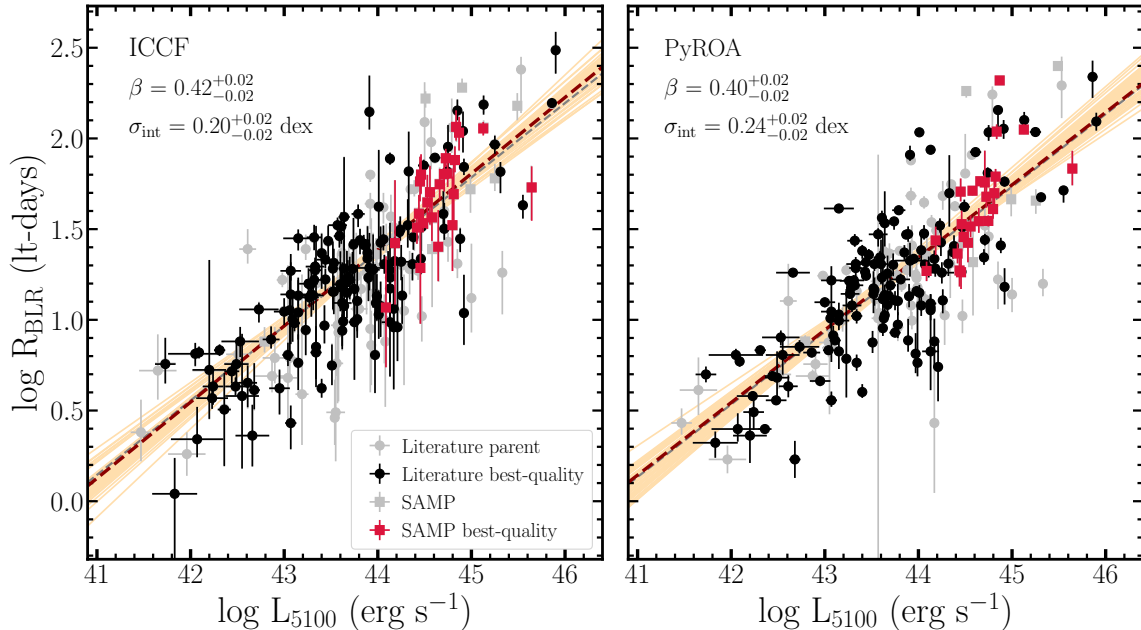


Figure 5. $R_{\text{BLR}}-L_{5100}$ relation based on ICCF (left) and PyROA (right). The sample presented here includes positive lags from the literature parent sample (grey filled circles) as well as the 30 positive lags from SAMP (Woo et al. 2024, grey open circles). The black filled and open circles represent the best-quality literature sample (see §3.5 for details) and the good-quality lags selected by Woo et al. (2024, black open circles). The grey and brown dashed lines represent the best-fit relations for the combined total and combined best-quality subsample, respectively. The orange lines are 50 randomly drawn realizations from the MCMC samples for illustrating the dispersion of the relation. The best-fit slope β and the intrinsic scatter σ_{int} are labeled in the legend.

et al. 2022, Guo et al., in preparation), obtaining the statistical significance of the correlation of two red-noise like signals. In this work we generate the p -value based on white-noise-like random light curves, which is a more conservative approach compared to $p(r_{\text{max}})$. Detailed comparison between these two approaches is beyond the scope of this work and will be explored in the future.

For consistency, we apply the same criteria for SAMP AGNs as we do for the literature sample, i.e., relaxing the first threshold to $r_{\text{max}} > 0.55$ and recalculating the p -values based on our methodology. We find that all the good-quality lag measurements from SAMP satisfy these two requirements. The third criterion is the same between this work and Woo et al. (2024). Upon our visual inspection, we also confirm the high-quality lags identified by Woo et al. (2024).

Note that we disqualify two objects from the best-quality measurements. One object is removed by requiring τ_{CCF} to be $1\sigma > 0$, and the other object is removed because its τ_{JAVELIN} is preferred than τ_{CCF} (Woo et al. 2024). Thus, we finalize 23 AGNs from SAMP as best-quality measurements for the following analysis.

3.6. Effect of the Uncertainty and Quality of Lag Measurements on the $R_{\text{BLR}}-L_{5100}$ Relation

In this section, we investigate the $R_{\text{BLR}}-L_{5100}$ relation using the total sample and the best-quality subsample, respectively, to investigate the effect of the lag measurement quality. Note that we only utilize the positive lags that are $1\sigma > 0$ in the fitting. We fit the $R_{\text{BLR}}-L_{5100}$ relation using the following form:

$$y = \alpha + \beta(x - x_0) \quad (1)$$

where x is an independent and y is a dependent variable. In the expression, the independent variable x is normalized according to its average x_0 , which equals to 43.89 for $\log L_{5100}$ in our sample. To determine the best-fit parameters, we utilize the MCMC analysis implemented by `emcee`¹ package (Foreman-Mackey et al. 2013), where the likelihood \mathcal{L} is expressed by:

$$\ln \mathcal{L}^2 = -\frac{1}{2} \sum_{i=1}^N \frac{(y_i - m_i)^2}{s_i^2} + \ln(2\pi s_i^2) \quad (2)$$

where the y_i and m_i are observation and model predictions of the i th object. The s_i is expressed as

$$s_i^2 = (\beta x_{\text{err}})^2 + y_{\text{err}}^2 + \sigma_{\text{int}}^2 \quad (3)$$

¹ <https://github.com/dfm/emcee>

where the last term σ_{int} is added to represent the intrinsic scatter of the relation. This is similar to other regression methods in the literature, e.g., LINMIX (Kelly 2007). In `emcee` calculation, we adopt flat prior distributions within reasonable parameter space. The best-fit values are determined as the median of the posterior distribution, with uncertainties represented by the range between the 16th and 84th percentiles.

In Figure 5 we present the $R_{\text{BLR}}-L_{5100}$ relation derived from the total sample as well as the best-quality subsample. Based on τ_{ICCF} , the best-fit relation for the best-quality subsample is described as:

$$\log R_{\text{BLR}} = 1.34 + 0.42 (\log L_{5100} - 43.89) \quad (4)$$

A consistent relation is found when we adopt τ_{PyROA} in the analysis (see Table 3). When we only include the best-quality AGNs, the slope is still in agreement within 1σ uncertainty with that for the total sample. Our result is aligned with the findings by Woo et al. (2024) who performed a similar analysis by collecting $H\beta$ lags from the literature (see also Malik et al. 2023; GRAVITY Collaboration et al. 2024a). Our analysis confirms that the flattening of $R_{\text{BLR}}-L_{5100}$ relation is real and remains consistent even after remeasuring $H\beta$ lags based on our uniform analysis and after selecting the best-quality subsample.

Table 3. $R_{\text{BLR}}-L_{5100}$ Relations Using the Total and Best-Quality Subsample Based on ICCF and PyROA

method	sample	β	α	σ_{int}
ICCF	total	$0.41^{+0.02}_{-0.02}$	$1.33^{+0.02}_{-0.02}$	$0.23^{+0.01}_{-0.01}$
	best-quality	$0.42^{+0.02}_{-0.02}$	$1.34^{+0.02}_{-0.02}$	$0.20^{+0.02}_{-0.02}$
PyROA	total	$0.40^{+0.02}_{-0.02}$	$1.29^{+0.02}_{-0.02}$	$0.25^{+0.01}_{-0.01}$
	best-quality	$0.40^{+0.02}_{-0.02}$	$1.30^{+0.02}_{-0.02}$	$0.24^{+0.02}_{-0.02}$

We observe a slight decrease in σ_{int} when we only include AGNs with the best-quality τ_{ICCF} , e.g., from 0.23 to 0.20 dex. The σ_{int} based on PyROA doesn't exhibit significant changes which is understandable since our quality selection focuses on τ_{ICCF} . In addition, the σ_{int} based on τ_{PyROA} is ~ 0.03 dex larger than that based on τ_{ICCF} , because of the smaller uncertainty of τ_{PyROA} . This demonstrates the influence of lag uncertainty on the σ_{int} of $R_{\text{BLR}}-L_{5100}$ relation. To our surprise, σ_{int} is only 0.25 dex even if we employ τ_{PyROA} and use the total sample. While the intrinsic scatter is not as small as it was measured a decade ago by Bentz et al. (2013), the current $R_{\text{BLR}}-L_{5100}$ relation is still relatively tight, especially considering that the current RM sample is

much larger and covers a broader range of Eddington ratio and luminosity.

4. THE DEPENDENCE ON VARIOUS LUMINOSITY TRACERS

In this section, we investigate the correlation of R_{BLR} with several luminosity tracers, i.e., the optical continuum luminosity L_{5100} , $H\beta$ luminosity $L_{H\beta}$, and [O III] luminosity $L_{[\text{O III}]}$. We use the best-quality subsample with τ_{ICCF} . In the case of AGNs with multiple lag measurements, we employ an average of them weighted by the uncertainties. From the 157 best-quality lags, we obtain 101 distinct AGNs in the average scheme, for which all three luminosity measures are available.

4.1. Luminosity Comparison

Table 4. $L_{H\beta}-L_{5100}$, and $L_{[\text{O III}]}-L_{5100}$ Relations in Average Scheme

relation	sample	β	α	σ_{int}
$L_{H\beta}-L_{5100}$	total	$0.94^{+0.02}_{-0.02}$	$42.32^{+0.02}_{-0.02}$	$0.14^{+0.01}_{-0.01}$
	$\lambda_{\text{Edd}} < 1.0$	$0.95^{+0.02}_{-0.02}$	$42.33^{+0.02}_{-0.02}$	$0.13^{+0.01}_{-0.01}$
$L_{[\text{O III}]}-L_{5100}$	total	$0.69^{+0.05}_{-0.05}$	$41.82^{+0.04}_{-0.04}$	$0.39^{+0.03}_{-0.03}$
	$\lambda_{\text{Edd}} < 1.0$	$0.72^{+0.05}_{-0.05}$	$41.84^{+0.04}_{-0.04}$	$0.38^{+0.03}_{-0.03}$

First, we examine the relation between L_{5100} , $L_{H\beta}$, and $L_{[\text{O III}]}$ in Figure 6 by employing the same MCMC linear regression method described in §3.6. In this context, $\log L_{5100}$ serves as an independent variable, while $\log L_{H\beta}$ and $\log L_{[\text{O III}]}$ act as a dependent variable. The pivot point, x_0 , is set as the median value of $\log L_{5100}$ for the total sample, i.e., 44.06 erg s^{-1} . We find the best-fit relation based on the total sample as:

$$\log L_{H\beta} = 42.32 + 0.94 (\log L_{5100} - 44.06) \quad (5)$$

$$\log L_{[\text{O III}]} = 41.82 + 0.69 (\log L_{5100} - 44.06) \quad (6)$$

The $L_{H\beta}-L_{5100}$ relationship is characterized by a small intrinsic scatter, $\sigma_{\text{int}} = 0.14^{+0.01}_{-0.01}$ dex, indicating that host-corrected L_{5100} is a good proxy for the Hydrogen ionizing continuum. The best-fit slope of $L_{H\beta}-L_{5100}$ relation, $\beta = 0.94^{+0.02}_{-0.02}$, is statistically smaller (3σ) than unity, indicating the presence of a weak Baldwin effect of $H\beta$. In contrast, the $L_{[\text{O III}]}-L_{5100}$ relation exhibits a substantially larger intrinsic scatter and a notably shallower slope, compared to the $L_{H\beta}-L_{5100}$ relation. It indicates a more pronounced Baldwin effect of [O III] relative to $H\beta$, which is consistent with the results from the large sample of SDSS (Shen & Ho 2014).

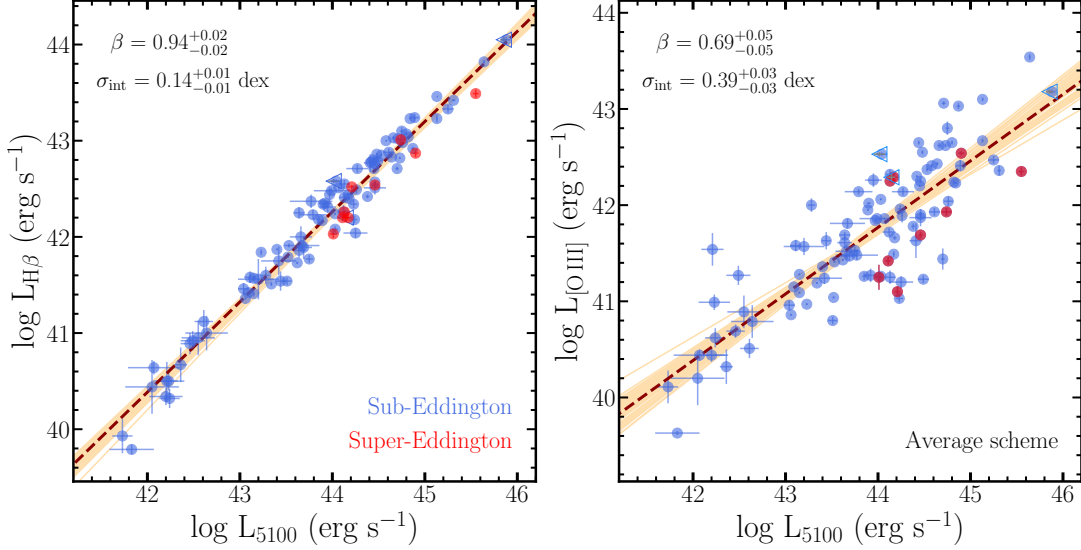


Figure 6. Comparison between different luminosity tracers in the average scheme. The left and right panel show the $L_{H\beta}$ - L_{5100} and $L_{[O III]}$ - L_{5100} relation, respectively. Sub- and super-Eddington ratios are displayed using blue and red color, respectively. The core-dominated radio-loud AGNs are highlighted by additional left-triangle envelopes. The brown dashed lines represent the best-fit relations, while the orange lines are randomly selected 50 realizations from the MCMC samples for illustrating the dispersion of the relation. In each panel, the best-fit slope β and the intrinsic scatter σ_{int} are labeled at the top left corner.

We next investigate the influence of Eddington ratio by dividing our sample into sub- and super-Eddington AGNs. Super-Eddington AGNs exhibit systematically lower $L_{H\beta}$ and $L_{[O III]}$ compared to sub-Eddington AGNs in Figure 6. To quantify this deviation, we obtain the best-fit relation for sub-Eddington and super-AGN subsamples as summarized in Table 4. The median deviation of super-Eddington AGNs is -0.21 dex in R_{BLR} from the best-fit $L_{H\beta}$ - L_{5100} relation of sub-Eddington AGNs, while that deviation is -1.00 dex for the $L_{[O III]}$ - L_{5100} relation. Note that super-Eddington AGNs are mostly high-luminosity AGNs (Figure 6), therefore the derived slope of $L_{H\beta}$ - L_{5100} relation is slightly shallower than the value measured by Dalla Bontà et al. (2020) (0.960 ± 0.020), whose sample mostly consists of sub-Eddington AGNs.

In addition, we explore other potential causes of the offset, for instance, the contamination of core-dominant radio-loud AGNs. Such objects may exhibit a large $L_{5100}/L_{H\beta}$ ratio due to the substantial jet-induced contamination in the continuum (e.g, Greene & Ho 2005). We compiled core-dominant radio-loud AGNs from literatures (e.g., Brotherton 1996). However, we find that these objects closely follow the $L_{H\beta}$ - L_{5100} relation of the rest of the objects, suggesting the R_{BLR} - L_{5100} relation is not strongly biased due to such objects.

4.2. $R_{\text{BLR}} - L$ Relation

Next, we investigate the $R_{\text{BLR}} - L$ relation using three different luminosity tracers, i.e., L_{5100} , $L_{H\beta}$, and $L_{[O III]}$.

We obtain the best-fit relations in the average scheme as

$$\log R_{\text{BLR}} = 1.41 + 0.43 (\log L_{5100} - 44.06) \quad (7)$$

$$\log R_{\text{BLR}} = 1.42 + 0.45 (\log L_{H\beta} - 42.33) \quad (8)$$

$$\log R_{\text{BLR}} = 1.32 + 0.49 (\log L_{[O III]} - 41.69) \quad (9)$$

with an intrinsic scatter, $0.18^{+0.02}_{-0.02}$, $0.17^{+0.02}_{-0.02}$, and $0.25^{+0.02}_{-0.02}$ dex, respectively for $R_{\text{BLR}}-L_{5100}$, $R_{\text{BLR}}-L_{H\beta}$, and $R_{\text{BLR}}-L_{[O III]}$ relation (see Figure 7 and Table 5). The $R_{\text{BLR}}-L_{H\beta}$ relation shows the smallest intrinsic scatter as expected because the $H\beta$ line emission is a direct product of the BLR Hydrogen ionization and is less subject to defects in host corrections. It suggests that $L_{H\beta}$ can serve as a good alternative to L_{5100} for the future $R_{\text{BLR}}-L$ relation analysis. On the other hand, the $R_{\text{BLR}}-L_{[O III]}$ relation exhibits a larger intrinsic scatter, which is also expected because $[O III]$ comes from the NLR, which covers a much larger scale. Consequently, its variability time scale should also be much longer than that of broad emission lines (e.g., Peterson et al. 2013).

As for the slope, we find that the slope varies when using different luminosity tracers. The $R_{\text{BLR}}-L_{5100}$ relation displays a slope of $0.43^{+0.02}_{-0.02}$, while the $R_{\text{BLR}}-L_{H\beta}$ relation shows a slope of $\beta = 0.45^{+0.03}_{-0.03}$. The small difference is partly due to the weak $H\beta$ Baldwin effect, i.e., higher-luminosity AGNs have slightly lower $L_{H\beta} / L_{5100}$ ratios. In the case of the $R_{\text{BLR}}-L_{[O III]}$ relation, the best-fit slope is $\beta = 0.49^{+0.04}_{-0.04}$. The derived slope

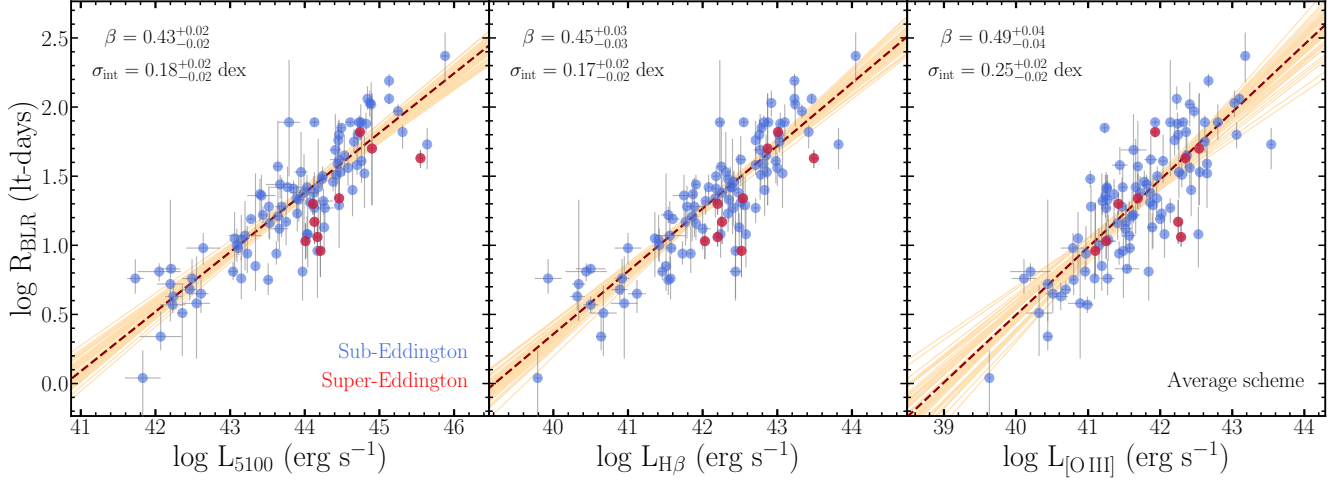


Figure 7. R_{BLR} as a function of different luminosity tracers in the average scheme, including L_{5100} (left), $L_{\text{H}\beta}$ (middle), and $L_{[\text{O III}]}$ (right). Sub- and super-Eddington objects are displayed using blue and red color, respectively. The brown dashed lines represent the best-fit relations of the total sample, and the orange lines are randomly selected 50 realizations from the MCMC samples for illustrating the dispersion of the relation. In each panel, the best-fit slope β and the intrinsic scatter σ_{int} of the relation is presented at the upper-left corner.

Table 5. $R_{\text{H}\beta}-L_{5100}$, $R_{\text{H}\beta}-L_{\text{H}\beta}$, and $R_{\text{H}\beta}-L_{[\text{O III}]}$ Relations in Average Scheme

Relation	Sample	x_0	β	α	σ_{int}
$R_{\text{BLR}}-L_{5100}$	total	44.06	$0.43^{+0.02}_{-0.02}$	$1.41^{+0.02}_{-0.02}$	$0.18^{+0.02}_{-0.02}$
	$\lambda_{\text{Edd}} < 1.0$	44.06	$0.45^{+0.02}_{-0.02}$	$1.43^{+0.02}_{-0.02}$	$0.16^{+0.02}_{-0.02}$
$R_{\text{BLR}}-L_{\text{H}\beta}$	total	42.33	$0.45^{+0.03}_{-0.03}$	$1.42^{+0.02}_{-0.02}$	$0.17^{+0.02}_{-0.02}$
	$\lambda_{\text{Edd}} < 1.0$	42.33	$0.46^{+0.03}_{-0.03}$	$1.43^{+0.02}_{-0.02}$	$0.16^{+0.02}_{-0.02}$
$R_{\text{BLR}}-L_{[\text{O III}]}$	total	41.69	$0.49^{+0.04}_{-0.04}$	$1.32^{+0.03}_{-0.03}$	$0.25^{+0.02}_{-0.02}$
	$\lambda_{\text{Edd}} < 1.0$	41.69	$0.50^{+0.04}_{-0.04}$	$1.33^{+0.03}_{-0.03}$	$0.24^{+0.02}_{-0.02}$

is somewhat smaller than the previously reported slope based on a smaller (0.61 ± 0.07 ; Greene et al. 2010). The difference is mainly related to the large difference in sample size. For instance, the inclusion of strong radio loud AGNs in our sample, e.g., PG 1100+772, which may have enhanced jet-induced [O III] emission (McIntosh et al. 1999), results in a smaller slope.

Finally, we investigate the influence of Eddington ratio by comparing sub-Eddington and super-Eddington AGNs. Super-Eddington objects show substantial deviations in both $R_{\text{BLR}}-L_{5100}$ and $R_{\text{BLR}}-L_{\text{H}\beta}$ relations (see Figure 7). These results are consistent with Du et al. (2015), who used a smaller sample (see also Woo et al. 2024). We quantify the deviation by obtaining the best-fit relation using only sub-Eddington AGNs (see Table 5). The median deviation (in R_{BLR}) of super-Eddington AGNs is -0.29 dex from the best-fit $R_{\text{BLR}}-L_{5100}$ relation of sub-Eddington AGNs, while the deviation is -0.21 dex in the $R_{\text{BLR}}-L_{\text{H}\beta}$ relation. In contrast, super-Eddington AGNs offset by only -0.07 dex in the $R_{[\text{O III}]}-L_{5100}$ relation. Consequently, while the intrinsic scatter of the $L_{5100}-L_{[\text{O III}]}$ relation is ~ 0.4 dex, the σ_{int}

of $R_{\text{BLR}}-L$ relation increases by 0.07 dex when L_{5100} is replaced with $L_{[\text{O III}]}$.

5. DISCUSSION

5.1. Super-Eddington vs. Sub-Eddington AGNs

We confirm that super-Eddington AGNs show deviation in both $R_{\text{BLR}}-L_{5100}$ and $R_{\text{BLR}}-L_{\text{H}\beta}$ relation (§ 4.2), which is consistent with Du et al. (2015). This deviation may be caused by various factors (see the discussion by Woo et al. 2024), including the self-shadowing effects associated with the slim disk (Wang et al. 2014b), the non-linear relation between optical and ionizing continua (Fonseca Alvarez et al. 2020), or the influence of BH spin (e.g., Czerny et al. 2019). We also demonstrate that the $R_{\text{BLR}}-L_{[\text{O III}]}$ relation, on the contrary, don't show such a deviation. In other words, for a given [O III] luminosity, sub-Eddington and super-Eddington AGNs do not exhibit distinct R_{BLR} statistically. We discuss several possibilities that can lead to the different trends.

First, it could be due to the long timescale required for [O III] to respond to central variability, which could be $\gg 10^3$ years. Its luminosity only reflects an av-

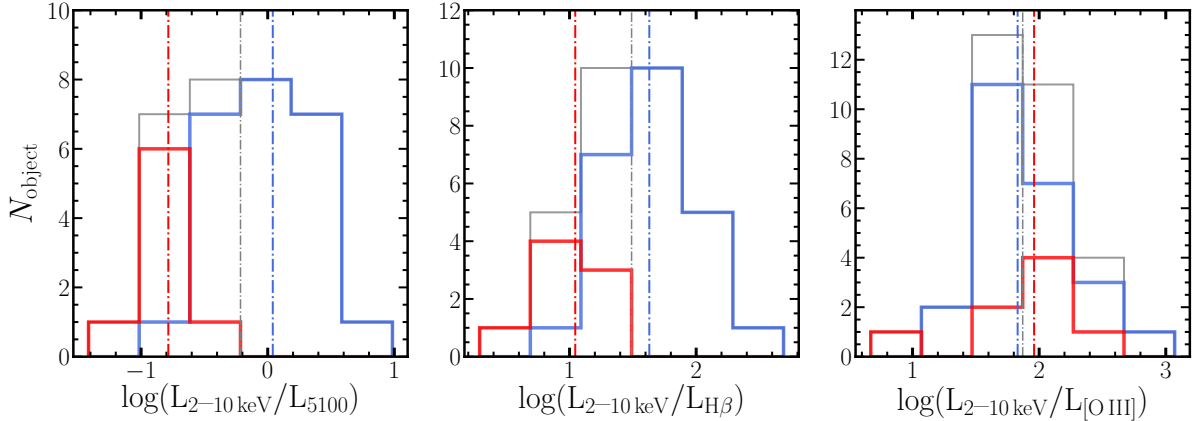


Figure 8. Histograms of the ratios of hard X-ray luminosity $L_{2-10\text{ keV}}$ to L_{5100} (left), $L_{H\beta}$ (middle), and $L_{[\text{O III}]}$ (right) based on a sample of 32 AGNs with hard X-ray luminosity available in Liu et al. (2021). The blue and red histograms represent the distribution of low and high λ_{Edd} subsample, respectively, with the division set as $\log\lambda_{\text{Edd}} \sim -0.3$. The vertical dashed lines in blue and red color indicate the median ratios for sub- and super-Eddington subsample, respectively. The grey histograms and vertical lines are the results for the total sample.

erage accretion rate over a long period, during which AGNs are likely in a sub-Eddington phase for most of the time. Consequently, the $[\text{O III}]$ luminosity of super-Eddington AGNs may under-represent the current accretion rate. This effect may compensate intrinsically shortened R_{BLR} in super-Eddington AGNs due to aforementioned factors, resulting in the lack of clear deviation between super- and sub-Eddington AGNs.

Second, it could indicate that R_{BLR} is determined by higher-energy photons, given that the ionizing potential of $[\text{O III}]$ is approximately 55 eV, while that for hydrogen is 13.6 eV. This scenario, combined with the assumption that the SED in far UV (FUV) to extreme UV (EUV) range is softer in super-Eddington AGNs than in sub-Eddington AGNs, can naturally explain all observations, including the lack of deviation in $R_{\text{BLR}}-L_{[\text{O III}]}$ relation, and the presence of deviation in $R_{\text{BLR}}-L_{H\beta}$ relation, and the even larger deviation in $R_{\text{BLR}}-L_{5100}$ relation. However, examining the EUV SED is challenging due to observational limitations. If we seek theoretical models for explanation, we find that the slim disk model indeed predicts a saturation of emission at EUV wavelengths as the accretion rate increases above several times of the Eddington limits (see Figure 8 in Kubota & Done 2019). In contrast, the FUV and optical emissions are less affected, resulting in a softer FUV to EUV SED in super-Eddington AGNs.

To distinguish these possibilities, we compile the 2 to 10 keV hard X-ray luminosity ($L_{2-10\text{ keV}}$) and study the $R_{H\beta}-L_{2-10\text{ keV}}$ relation. This idea is based on the observation that the hard X-ray emission in super-Eddington AGNs is also relatively weak (e.g., Liu et al. 2021), while it is not subject to the long-timescale issue as for $L_{[\text{O III}]}$. In Figure 8, we present the distributions of the ratio

between $L_{2-10\text{ keV}}$ and optical luminosities based on a sample of 32 AGNs, for which $L_{2-10\text{ keV}}$ are available in Liu et al. (2021). Because of the limited sample size, we use $\log\lambda_{\text{Edd}} = -0.3$ to divide low- λ_{Edd} and high- λ_{Edd} subsamples. We find that high- λ_{Edd} AGNs exhibit smaller $L_{2-10\text{ keV}}/L_{5100}$ and $L_{2-10\text{ keV}}/L_{H\beta}$ ratios compared to low- λ_{Edd} AGNs. The median differences are 0.83 dex and 0.59 dex for these two ratios, respectively. On the contrary, low- λ_{Edd} and high- λ_{Edd} AGNs only show a small difference, with a median of 0.13 dex, in the $L_{2-10\text{ keV}}/L_{[\text{O III}]}$ ratio.

Figure 9 presents the relation between R_{BLR} and $L_{2-10\text{ keV}}$ for these 32 AGNs, compared to the relations based on other luminosity tracers. Low and high- λ_{Edd} AGNs show only 0.08 dex deviation in the $R_{\text{BLR}}-L_{2-10\text{ keV}}$ relation, which is similar to the case of $L_{[\text{O III}]}$. We also find that the σ_{int} of $R_{\text{BLR}}-L_{2-10\text{ keV}}$ relation remains consistent with or without including high- λ_{Edd} AGNs (see Figure 9). On the contrary, the deviation is substantial in the $R_{\text{BLR}}-L_{5100}$ relation as well as the $R_{\text{BLR}}-L_{H\beta}$ relation (similar to the results presented in §4.2 based on larger sample). Regarding the slopes, all of the slopes are larger than those reported in Figure 7 based on larger sample, which is mainly due to the large difference in sample size and potential sample selection effect.

These results can be considered as evidence of the EUV SED scenario, given that the hard X-ray emission in AGNs is mainly originated from EUV photons through inverse Comptonization. In other words, the same EUV photons that are responsible for generating hard X-ray emission could also determine R_{BLR} . The larger-than-0.5 slope, if confirmed, could be resulted from the non-linear interaction between the disk and

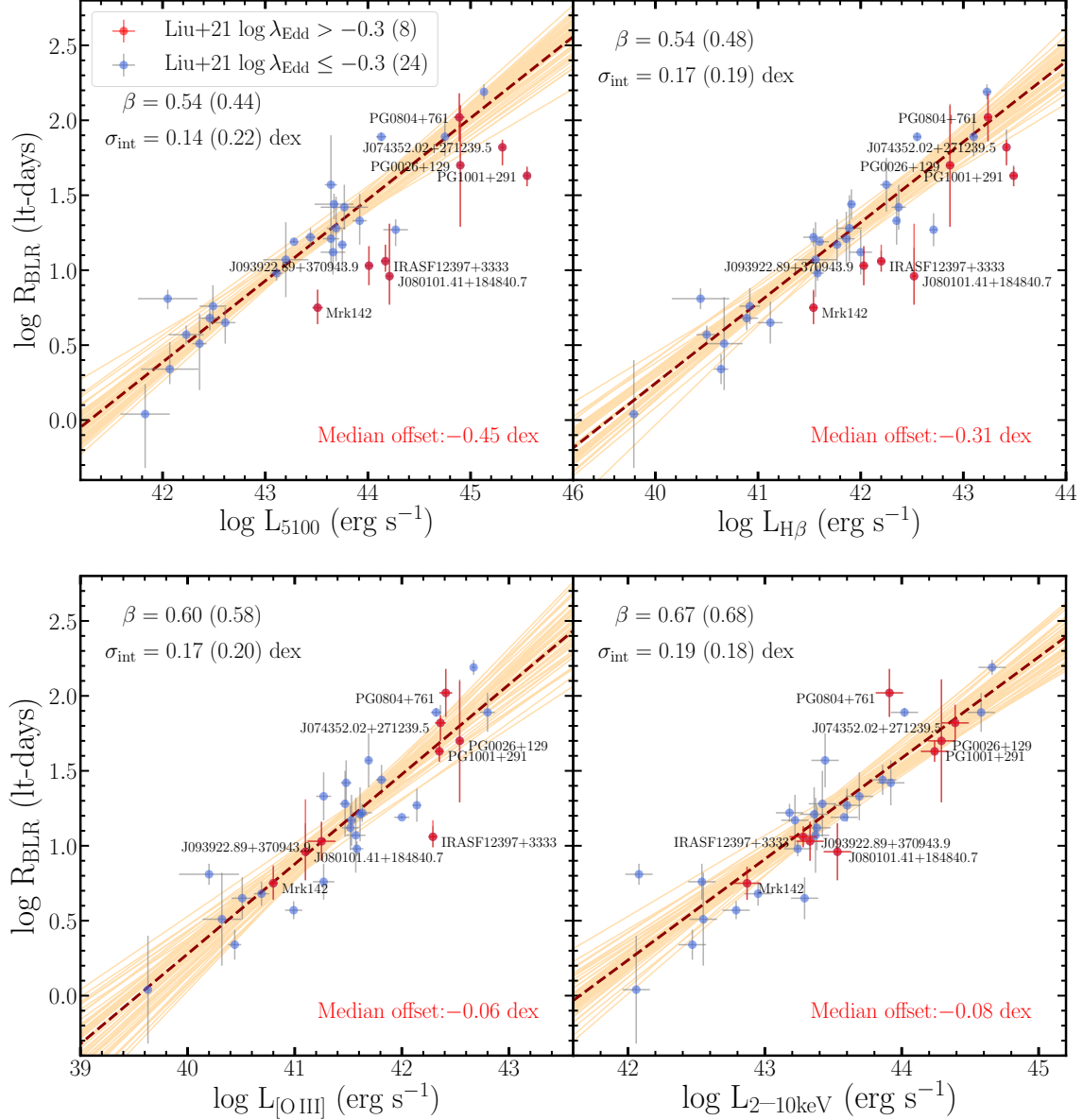


Figure 9. The $R_{\text{BLR}}-L$ relation for the sample with X-ray luminosity measured by Liu et al. (2021). The relation based on L_{5100} (upper left), $L_{\text{H}\beta}$ (upper right), $L_{[\text{O III}]}$ (lower left), and $L_{2-10\text{keV}}$ (lower right) are presented. Twenty-four low and eight high- λ_{Edd} AGNs (divided by $\log \lambda_{\text{Edd}} = -0.3$) are shown in blue and red color, respectively. The name of each high λ_{Edd} AGN is given for comparing their different offset in different panels. The brown dashed lines represent the best-fit relations of the sub-Eddington subsample while the orange lines are randomly selected 50 realizations from the MCMC samples for illustrating the dispersion of the relation. The best-fit slope β and the intrinsic scatter σ_{int} for the low- λ_{Edd} subsample are presented at the upper-left corner, while the values in the brackets represent the results for the total sample.

corona (e.g., Lusso et al. 2010), where more luminosity AGNs tend to have smaller hard X-ray to optical/UV flux ratios. The results from Figure 9 actually reveal a connection among the hard X-ray emission from the innermost region, the BLR sizes, and [O III] emission from the narrow line region, which cannot be easily explained by the properties of a single component, such as BLR

density or BLR emission anisotropy. The ionizing SED provides a natural explanation.

The recent results from GRAVITY show that both the torus size – L relation and BLR size – L relation show a slope of ~ 0.5 (GRAVITY Collaboration et al. 2024a,b) using hard X-ray luminosity, while they exhibit a slope of ~ 0.4 using L_{5100} (e.g., Gravity Collaboration et al. 2023; GRAVITY Collaboration et al. 2024b; Chen et al.

2023; Mandal et al. 2024). While the slope is smaller than what we measured here due to either sample selection effects or systematics between RM and interferometric observations, the results demonstrate the critical role of the ionizing SED in determining the slope of the $R_{\text{BLR}}-L$ relation.

While the $L_{2-10\text{keV}}$ is not subject to timescale issues, it is not measured simultaneously with R_{BLR} . The large variability of X-ray can result in a large scatter and erase any small deviation. Nonetheless, we find that the σ_{int} of the $R_{\text{BLR}}-L_{2-10\text{keV}}$ relation is not large (0.18 dex, if assuming the uncertainty of $L_{2-10\text{keV}}$ as 0.10 dex). Liu et al. (2021) only adopted high state X-ray observations, which could be a potential reason for the small scatter. It is also possible that with larger sample size, the σ_{int} will increase. The $R_{\text{BLR}}-L_{2-10\text{keV}}$ relation should be tested in the future with quasi-simultaneous X-ray and UV-optical observations.

5.2. Future Improvement

In this work, we investigated the influence of lag measurements and the choice of luminosity tracer on the $R_{\text{BLR}}-L$ relation. We discuss several future directions, which could improve the $R_{\text{BLR}}-L$ relation.

First, since the correction for the host contamination has not been homogeneously performed in measuring L_{5100} , a future direction is to perform uniform host decomposition for the entire RM sample using high resolution images, e.g., from the Hubble space telescope. This is difficult given the rapidly growing RM sample size. The use of $L_{\text{H}\beta}$ instead of L_{5100} may be a good alternative for studying the $R_{\text{BLR}}-L$ relation. However, the bias due to the Eddington ratio still affects the $R_{\text{BLR}}-L_{\text{H}\beta}$ relation.

Second, while the absence of the rest-frame extreme UV observations hinders understanding of AGN ionizing SED multi-band simultaneous observations may help improving our understanding of AGN SED. By combining quasi-simultaneous optical, near-UV, and soft X-ray observation, one may obtain relatively good constraints on the ionizing SED shape. Expanding these constraints to a larger RM sample, the systematic trend in the $R_{\text{BLR}}-L$ relation can be better understood. Alternatively, studying the far/near-UV to optical photometry of a large sample of high-redshift ($z > 2$) AGNs can also provide useful constraints (e.g., Zheng et al. 1997; Krawczyk et al. 2013).

Third, new RM campaigns can be carried out for AGNs with previous lag measurements, especially for those from early years with moderate or low cadence. The lags of some super-Eddington AGNs are suspected to be biased by their insufficient cadence (e.g., PG

0804+761). Thus, new campaign can provide consistency check and may reduce the scatter of the $R_{\text{BLR}}-L$ relation.

6. SUMMARY

In this paper we investigated the $\text{H}\beta$ lag measurements and the BLR size-luminosity relation using a large sample of AGNs. We summarize the main results as follows:

1. We remeasure the $\text{H}\beta$ lags for 212 AGNs in the literature using three different methods, i.e., ICCF, JAVELIN and PyROA. ICCF is the most reliable approach albeit with larger uncertainties compared to other methods. While τ_{JAVELIN} is consistent with τ_{ICCF} for most objects, it fails for some objects as the cross correlation result is trapped in the seasonal gaps or not converged. In the case of PyROA we obtained generally consistent lags but with smaller lag uncertainties compared to those of ICCF.
2. We obtain the best-fit $R_{\text{BLR}}-L_{5100}$ relation based on ICCF as $\log R_{\text{BLR}} = 1.34 + 0.42 (\log L_{5100} - 43.89)$, with an intrinsic scatter of $0.20^{+0.02}_{-0.02}$ dex, when combining the best-quality ICCF lags from literature sample and SAMP. Compared to the results without quality selection, the slope is consistent but the intrinsic scatter is slightly reduced. When τ_{PyROA} is used, we find generally consistent results with those based on ICCF but with slightly larger intrinsic scatter (~ 0.24 dex) due to its smaller lag uncertainty.
3. We investigate different luminosity tracers in the $R_{\text{BLR}}-L$ relation. We find that $\text{H}\beta$ show a weak Baldwin effect, while $[\text{O III}]$ exhibit a significant Baldwin effect. Super-Eddington AGNs have lower $L_{\text{H}\beta}$ and $L_{[\text{O III}]}$ at given L_{5100} , while the deviation is stronger in the $L_{[\text{O III}]}-L_{5100}$ relation.
4. In the average scheme, the best-fit slope increases from the $0.43^{+0.02}_{-0.02}$ for the $R_{\text{BLR}}-L_{5100}$ relation, to $0.45^{+0.03}_{-0.03}$ for the $R_{\text{BLR}}-L_{\text{H}\beta}$ relation, and to $0.49^{+0.04}_{-0.04}$ for $R_{\text{BLR}}-L_{[\text{O III}]}$ relation. The $R_{\text{BLR}}-L_{\text{H}\beta}$ relation exhibits a small σ_{int} (~ 0.17 dex), while the $R_{\text{BLR}}-L_{[\text{O III}]}$ relation shows a larger σ_{int} (~ 0.25 dex). The deviation of super-Eddington AGNs is significant in both $R_{\text{BLR}}-L_{5100}$ and $R_{\text{BLR}}-L_{\text{H}\beta}$ relations, while it is insignificant in the $R_{\text{BLR}}-L_{[\text{O III}]}$ relation.
5. We discuss several possibilities for the insignificant deviation between sub- and super-Eddington AGNs in the $R_{\text{BLR}}-L_{[\text{O III}]}$ relation, including the

[O III] variability time scale, the difference in the FUV to EUV SED. Based on a small sample of AGNs with $L_{2-10\text{ keV}}$ available, we find that the $R_{\text{BLR}}-L_{2-10\text{ keV}}$ relation also exhibits no significant difference between low- and high-Eddington ratio subsample (see §5.1 for details). Such observations could be considered as evidence supporting the ionizing SED scenario.

This work has been supported by the Basic Science Research Program through the National Research Foundation of Korean Government (2019R1A6A1A10073437 and 2021R1A2C3008486). We thank the anonymous referee for the helpful comments and suggestions. We thank Hengxiao Guo for initial light curve collection. We thank Donghoon Son, Hojin Cho, Amit Kumar Mandal, Jaejin Shin, Hengxiao Guo for lag quality assessment.

APPENDIX

A. LAG MEASUREMENTS

Table A.1 records the lag measurements and related parameters for the literature parent sample, while A.2 summarizes the lag measurements for SAMP. Table A.3 summarizes the lags and luminosities in the average scheme.

Table A.1. Lag measurements and quality parameters for literature parent sample

No.	Column	Format	Unit	Description
1	ID	Long		Object ID
2	Object	String		Object Name
3	Reference	String		Reference paper of the light curve and initial lag measurement
4	Redshift	Long		Redshift of the object
5	Rmax	Long		Maximum correlation coefficient r_{\max}
6	Rmax_DE	Long		Maximum correlation coefficient r_{\max} after detrending
7	p-value	Long		p -value from a cross-correlation reliability test
8	TAU_LITERATURE	Long	Days	Literature reported rest-frame lag measurement; -1 indicates not available
9	e_TAU_LITERATURE	Long	Days	Lower uncertainty of TAU_LITERATURE
10	E_TAU_LITERATURE	Long	Days	Upper uncertainty of TAU_LITERATURE
11	TAU_ICCF	Long	Days	Final rest-frame lag measurement based on ICCF centroids
12	e_TAU_ICCF	Long	Days	Lower uncertainty of TAU_ICCF
13	E_TAU_ICCF	Long	Days	Upper uncertainty of TAU_ICCF
14	Fpeak_ICCF	Long		f_{peak} of TAU_ICCF
15	Flag_Detrend_ICCF	Long		Flag for detrending: 1 means detrended while 0 means not detrended
16	Flag_Posterior_ICCF	Long		Flag on posterior distributions for ICCF centroids. 1 means good; 2 means not-converged; 3 means the primary peak is affected by the boarder of the lag searching window.
17	Visual_Inspection_ICCF	Long		Visual quality assessment of the TAU_ICCF, where 5 means the best quality, while 1 means less good quality.
18	TAU_JAVELIN	Long	Days	Final rest-frame lag measurement based on JAVELIN
19	e_TAU_JAVELIN	Long	Days	Lower uncertainty of TAU_JAVELIN
20	E_TAU_JAVELIN	Long	Days	Upper uncertainty of TAU_JAVELIN
21	Fpeak_JAVELIN	Long		f_{peak} of TAU_JAVELIN
22	Flag_Posterior_JAVELIN	Long		Flag on posterior distributions for JAVELIN. Same as Flag_Posterior_ICCF.
23	TAU_PyROA	Long	Days	Final rest-frame lag measurement based on PyROA
24	e_TAU_PyROA	Long	Days	Lower uncertainty of TAU_PyROA
25	E_TAU_PyROA	Long	Days	Upper uncertainty of TAU_PyROA
26	Fpeak_PyROA	Long		f_{peak} of TAU_PyROA
27	Flag_Posterior_PyROA	Long		Flag on posterior distributions for PyROA. Flag_Posterior_ICCF.
28	Flag_Best_Quality	Long		Equal 1: Selected; Equal 0: Not selected
29	LogL5100	Long	erg s^{-1}	Log luminosity at 5100\AA
30	e_LogL5100	Long	erg s^{-1}	Uncertainty of LogL5100
31	FWHM_mean	Long	km s^{-1}	Collected FWHM from mean spectra; -1 indicates not available
32	e_FWHM_mean	Long	km s^{-1}	Uncertainty of FWHM_mean
33	Sigma_rms	Long	km s^{-1}	Collected σ_{line} from rms spectra; -1 indicates not available
34	e_Sigma_rms	Long	km s^{-1}	Uncertainty of Sigma_rms

Table A.2. Lag measurements and quality parameters for SAMP sample

No.	Column	Format	Unit	Description
1	Object	String		Object Name
2	Redshift	Long		Redshift of the object
3	TAU_ICCF	Long	Days	Final observed-frame lag measurement based on ICCF (centroids)
4	e_TAU_ICCF	Long	Days	Lower uncertainty of TAU_ICCF
5	E_TAU_ICCF	Long	Days	Upper uncertainty of TAU_ICCF
6	Fpeak_ICCF	Long		f_{peak} of TAU_ICCF
7	TAU_JAVELIN	Long	Days	Final observed-frame lag measurement based on JAVELIN
8	e_TAU_JAVELIN	Long	Days	Lower uncertainty of TAU_JAVELIN
9	E_TAU_JAVELIN	Long	Days	Upper uncertainty of TAU_JAVELIN
10	Fpeak_JAVELIN	Long		f_{peak} of TAU_JAVELIN
11	TAU_PyROA	Long	Days	Final observed-frame lag measurement based on PyROA
12	e_TAU_PyROA	Long	Days	Lower uncertainty of TAU_PyROA
13	E_TAU_PyROA	Long	Days	Upper uncertainty of TAU_PyROA
14	Fpeak_PyROA	Long		f_{peak} of TAU_PyROA
15	Flag_Best_Quality_ICCF	Long		Flag indicates the final selected best-quality sample based on ICCF. Equal 1: selected best-quality ones; Equal 0: not selected.
16	LogL5100	Long	erg s^{-1}	Log luminosity at 5100Å
17	e_LogL5100	Long	erg s^{-1}	Uncertainty of LogL5100

Table A.3. Lags and Luminosities in the Average Scheme

No.	Column	Format	Unit	Description
1	Object	String		Object Name
2	Redshift	Long		Redshift of the object
3	LogR	Long	lt-days	Log BLR Radius
4	e_LogR	Long	lt-days	Lower uncertainty of LogR
5	E_LogR	Long	lt-days	Upper uncertainty of LogR
6	LogL5100	Long	erg s^{-1}	Log AGN luminosity at 5100Å
7	e_LogL5100	Long	erg s^{-1}	Uncertainty of LogL5100
8	LogLHbeta	Long	erg s^{-1}	Log Luminosity of Broad H β ; -1 indicates not available
9	e_LogLHbeta	Long	erg s^{-1}	Uncertainty of LogLHbeta
10	LogLOIII	Long	erg s^{-1}	Log luminosity of [O III]; -1 indicates not available
11	e_LogLOIII	Long	erg s^{-1}	Uncertainty of LogLOIII
12	LogL2-10keV	Long	erg s^{-1}	Log Hard X-ray luminosity at 2-10 keV; -1 indicates not available
13	LogLambda_Edd	Long		Log Eddington Ratio
14	e_LogLambda_Edd	Long		Lower uncertainty of LogLambda_Edd
15	E_LogLambda_Edd	Long		Upper uncertainty of LogLambda_Edd

REFERENCES

- Bentz, M. C., Denney, K. D., Grier, C. J., et al. 2013, *ApJ*, 767, 149
- Blandford, R. D., & McKee, C. F. 1982, *ApJ*, 255, 419
- Brotherton, M. S. 1996, *ApJS*, 102, 1
- Chen, Y.-J., Liu, J.-R., Zhai, S., et al. 2023, *MNRAS*, 522, 3439
- Collin, S., Kawaguchi, T., Peterson, B. M., & Vestergaard, M. 2006, *A&A*, 456, 75
- Czerny, B., Wang, J.-M., Du, P., et al. 2019, *ApJ*, 870, 84
- Dalla Bontà, E., Peterson, B. M., Bentz, M. C., et al. 2020, *ApJ*, 903, 112
- Donnan, F. R., Horne, K., & Hernández Santisteban, J. V. 2021, *MNRAS*, 508, 5449
- Du, P., & Wang, J.-M. 2019, *ApJ*, 886, 42
- Du, P., Hu, C., Lu, K.-X., et al. 2014, *ApJ*, 782, 45
- . 2015, *ApJ*, 806, 22
- Du, P., Lu, K.-X., Zhang, Z.-X., et al. 2016, *ApJ*, 825, 126
- Du, P., Brotherton, M. S., Wang, K., et al. 2018, *ApJ*, 869, 142
- Ferrarese, L., & Merritt, D. 2000, *ApJL*, 539, L9
- Fonseca Alvarez, G., Trump, J. R., Homayouni, Y., et al. 2020, *ApJ*, 899, 73
- Foreman-Mackey, D., Hogg, D. W., Lang, D., & Goodman, J. 2013, *PASP*, 125, 306
- Gaskell, C. M., & Peterson, B. M. 1987, *ApJS*, 65, 1
- Gebhardt, K., Bender, R., Bower, G., et al. 2000, *ApJL*, 539, L13
- Gravity Collaboration, Amorim, A., Bourdarot, G., et al. 2023, *A&A*, 669, A14
- GRAVITY Collaboration, Amorim, A., Bourdarot, G., et al. 2024a, arXiv e-prints, arXiv:2401.07676
- . 2024b, arXiv e-prints, arXiv:2407.13458
- Greene, J. E., & Ho, L. C. 2005, *ApJ*, 630, 122
- Greene, J. E., Hood, C. E., Barth, A. J., et al. 2010, *ApJ*, 723, 409
- Grier, C. J., Trump, J. R., Shen, Y., et al. 2017, *ApJ*, 851, 21
- Grier, C. J., Shen, Y., Horne, K., et al. 2019, *ApJ*, 887, 38
- Gültekin, K., Richstone, D. O., Gebhardt, K., et al. 2009, *ApJ*, 698, 198
- Häring, N., & Rix, H.-W. 2004, *ApJL*, 604, L89
- Homayouni, Y., Trump, J. R., Grier, C. J., et al. 2020, *ApJ*, 901, 55
- Hu, C., Li, S.-S., Yang, S., et al. 2021, *ApJS*, 253, 20
- Kaspi, S., Smith, P. S., Netzer, H., et al. 2000, *ApJ*, 533, 631
- Kelly, B. C. 2007, *ApJ*, 665, 1489
- Kelly, B. C., Bechtold, J., & Siemiginowska, A. 2009, *ApJ*, 698, 895
- Khatu, V. C., Gallagher, S. C., Horne, K., et al. 2023, *ApJ*, 958, 127
- Krawczyk, C. M., Richards, G. T., Mehta, S. S., et al. 2013, *ApJS*, 206, 4
- Kubota, A., & Done, C. 2019, *MNRAS*, 489, 524
- Li, J., Silverman, J. D., Ding, X., et al. 2021, *ApJ*, 922, 142
- Li, I-Hsiu, J., Shen, Y., Brandt, W. N., et al. 2019, *ApJ*, 884, 119
- Li, Y.-R., Zhang, Z.-X., Jin, C., et al. 2020, *ApJ*, 897, 18
- Liu, H., Luo, B., Brandt, W. N., et al. 2021, *ApJ*, 910, 103
- Lusso, E., Comastri, A., Vignali, C., et al. 2010, *A&A*, 512, A34
- Magorrian, J., Tremaine, S., Richstone, D., et al. 1998, *AJ*, 115, 2285
- Malik, U., Sharp, R., Penton, A., et al. 2023, *MNRAS*, 520, 2009
- Mandal, A. K., Woo, J.-H., Wang, S., et al. 2024, *ApJ*, 968, 59
- Marconi, A., & Hunt, L. K. 2003, *ApJL*, 589, L21
- McIntosh, D. H., Rieke, M. J., Rix, H. W., Foltz, C. B., & Weymann, R. J. 1999, *ApJ*, 514, 40
- Park, D., Woo, J.-H., Treu, T., et al. 2012, *ApJ*, 747, 30
- Peterson, B. M. 1993, *PASP*, 105, 247
- Peterson, B. M., Pogge, R. W., Wanders, I., Smith, S. M., & Romanishin, W. 1995, *PASP*, 107, 579
- Peterson, B. M., Wanders, I., Horne, K., et al. 1998, *PASP*, 110, 660
- Peterson, B. M., Ferrarese, L., Gilbert, K. M., et al. 2004, *ApJ*, 613, 682
- Peterson, B. M., Denney, K. D., De Rosa, G., et al. 2013, *ApJ*, 779, 109
- Shen, Y., & Ho, L. C. 2014, *Nature*, 513, 210
- Shen, Y., & Liu, X. 2012, *ApJ*, 753, 125
- Shen, Y., Richards, G. T., Strauss, M. A., et al. 2011, *ApJS*, 194, 45
- Shen, Y., Hall, P. B., Horne, K., et al. 2019, *ApJS*, 241, 34
- Shen, Y., Grier, C. J., Horne, K., et al. 2023, arXiv e-prints, arXiv:2305.01014
- Sun, M., Grier, C. J., & Peterson, B. M. 2018
- U, V., Barth, A. J., Vogler, H. A., et al. 2022, *ApJ*, 925, 52
- Vestergaard, M., & Peterson, B. M. 2006, *ApJ*, 641, 689
- Wang, J.-M., Qiu, J., Du, P., & Ho, L. C. 2014a, *ApJ*, 797, 65
- Wang, J.-M., Du, P., Hu, C., et al. 2014b, *ApJ*, 793, 108
- Wang, S., Shen, Y., Jiang, L., et al. 2019, *ApJ*, 882, 4
- . 2020, *ApJ*, 903, 51
- Woo, J.-H., & Urry, C. M. 2002, *ApJ*, 579, 530
- Woo, J.-H., Yoon, Y., Park, S., Park, D., & Kim, S. C. 2015, *ApJ*, 801, 38

- Woo, J.-H., Treu, T., Barth, A. J., et al. 2010, *ApJ*, 716, 269
- Woo, J.-H., Son, D., Gallo, E., et al. 2019, *Journal of Korean Astronomical Society*, 52, 109
- Woo, J.-h., Wang, S., Rakshit, S., et al. 2024, *The Astrophysical Journal*, 962, 67.
<http://dx.doi.org/10.3847/1538-4357/ad132f>
- Yu, L.-M., Bian, W.-H., Zhang, X.-G., et al. 2020a, *ApJ*, 901, 133
- Yu, Z., Kochanek, C. S., Peterson, B. M., et al. 2020b, *MNRAS*, 491, 6045
- Zhang, Z.-X., Du, P., Smith, P. S., et al. 2019, *ApJ*, 876, 49
- Zheng, W., Kriss, G. A., Telfer, R. C., Grimes, J. P., & Davidsen, A. F. 1997, *ApJ*, 475, 469
- Zu, Y., Kochanek, C. S., & Peterson, B. M. 2011, *ApJ*, 735, 80